# Independent estimates of carbon stocks in croplands: UAV-LiDAR and machine learning vs. eddy-covariance

**Jaime C. Revenga[1], Katerina Trepekli[1], Rasmus Jensen[1], Pauline S. Rummel[1], Thomas Friborg[1]**

[1]Department of Geosciences and Natural Resources Management (IGN), Copenhagen University, Denmark
[1]Østervolgade, 10, 1350 Copenhagen, Denmark

**Key Points:**

- The plant carbon budget in croplands estimated from UAV-LiDAR and machine learning regression is comparable with the carbon ecosystem uptake estimated via the eddy covariance technique.

- The relative match between the UAV-based method and the flux-based method along the two growing seasons (2.5 ± 10.4 % in 2020, and -9.0 ± 13.3 % in 2021) indicates that the UAV-based method is a valuable tool for plant carbon stock assessments, adaptive crop management practice and nutrient cycling studies in croplands.

- The presented method has the potential to estimate cumulative $CO_2$ fluxes over areas not covered by direct eddy-covariance flux measurements.

Corresponding author: Jaime C. Revenga, `contact: jar@ign.ku.dk`

## Abstract

Understanding sequestration of organic carbon (C) in agroecosystems is of primary importance for greenhouse gas (GHG) accounting in managed ecosystems, as well as to allow informed land use management. However, a broader application of precise C accounting is currently constrained by a limited number of direct flux measurements. Aside well-studied ecosystems (via the eddy-covariance technique), many still bear significant margins of uncertainty. In this study, we aim to qualify a new method for estimating accumulated C stocks in agriculture sites, by predicting the above-ground carbon (AGC) of vegetation throughout the growing season using mobile platforms and machine learning (ML) regression methods. Then, we benchmark these estimates with $CO_2$ fluxes derived from the eddy-covariance method from the ICOS DK-Vng site in Denmark. We utilized a light detection and ranging (LiDAR) sensor onboard an unstaffed aerial vehicle (UAV) to derive the geometrical characteristics of crops, and we conducted in parallel destructive field-based measurements of AGC. Then, a ML pipeline was designed to provide estimates of AGC as a supervised regression problem, using the LiDAR-derived point cloud data as predicting features and the AGC labels as ground-truth target values. The ML model attained predictions of $R^2 = 0.71$ and R2 = 0.93 at spatial resolutions of 1 $m^2$ and 2 $m^2$, respectively. The C content in the above-ground plant components was assessed via laboratory analysis (46.6 ± 0.3% of C-to-biomass in barley and 47.7 ± 0.3% in wheat), while the below-ground components (root allocation and rhizodeposition) were estimated based on a phenology-dependent allometric ratio. The cumulative value of C uptake along the growing season (i.e. NPP) was compared with the difference of C predictions between every two UAV-LiDAR survey dates, finding an optimal disagreement between methods below ± 10% in two different crop types. Various experimental set-ups are evaluated as well as the sources of uncertainty issued from the sampling design.


---



---

# = Introduction =

The agricultural sector is the world's second-largest greenhouse gas (GHG) emitter, after the energy sector, accounting for a quarter of total global anthropogenic GHG emissions [1]. While agriculture is a driver of climate change, the observed climate alterations have in turn challenged the global crop productivity in the last decades [2, 3]. In the absence of technological adaptations and dedicated mitigation measures [4], the environmental effects of agricultural activities could increase by 50–90 % [5], and the global crop productivity might be reduced by 17 % by 2050 [6]. In most countries, the accounting of emissions for land-use and agriculture relies on simple upscaling of standardized values, with little to no data-driven validation procedures. This is hindering most accurate accounting as well as attaining efficient and precise solutions.

Monitoring carbon (C) sequestration and $CO_2$ emissions from croplands is a prerequisite for an effective design of sustainable agricultural management practice. It targets the reduction of agriculture's impact on the environment and improves the quantification of crops' carbon footprints, while optimizing crop yield [7]. However, the adoption of climate-resilient and low-emission practices in agriculture has not yet reached the recommended levels [5].

In a changing climate, different geographical locations exhibit contrasting extreme weather events such as high temperatures, drought or heavy precipitation, varying shifts in timing and length of growing seasons, or heat stress via temperature increases [8], highlighting the necessity to quantify carbon sequestration capacity with methods and technologies tailored to specific ecosystems' conditions. In this context, precision agriculture has been acknowledged as a promising set of methods in sustainable intensification programs, in order to close yield gaps [9, 10, 11] while reducing GHG emissions. In the last decades, precision agriculure has been successfully implemented for optimizing crop yield by monitoring variations of crop health status, above ground biomass, water availability, soil quality, or nutritient supply but the monitoring of carbon stock dynamics at fine spatio-temporal resolution and at the farm scale remains challenging.

The standard framework to account for the transit of atmospheric $CO_2$ at the ecosystem scale is the net ecosystem exchange (NEE, Figure 1) [12], which is the net exchange of $CO_2$ fluxes at the atmosphere-biosphere interface. NEE is calculated as the difference between $CO_2$ uptake (i.e. gross primary productivity, GPP) and release of $CO_2$ representing the ecosystem respiratory losses ($R_{eco}$) [12]. Another commonly used magnitude in ecosystem budgeting is the net primary productivity (NPP) that, compared to NEE, does not explicitly include soil-derived fluxes and heterotrophic respiration, therefore reflecting the photosynthetic productivity of vegetation alone [13]. Thus, NPP is the most direct surrogate measure for plant growth provided by the flux-based eddy covariance framework. Many studies in different regions have reported large interannual variability of NEE in croplands, acting either as carbon sinks [14], as sources [15, 16], or as relatively neutral [17]. This divergence in assessments suggest a limited undersanding and an opportunity for enhancement in the methods employed.

In carbon budgeting at the ecosystem scale, it is advisable to report a range of confidence levels for C estimates, rather than targeting a specific value [18]. This is due to the fact that ecosystem-level estimates are bound to co-ocurring complex phenomena, so that it is necessary to count on certain assumptions (e.g. negligible levels of lateral carbon fluxes and heterotrophic respiration, atmospheric turbulence conditions reached, etc.) which may compromise estimates' accuracy.

In order to assess the consistency of the net ecosystem carbon balance (NECB), established approaches involve comparing a measured quantity (e.g. NEE) obtained at the same temporal and spatial scale using independent methods [19, 20, 21, 22, 23]. This can be done via either: (i) micrometeorological methods to assess the ecosystem-atmosphere fluxes; (ii) inventories of stock changes in the biomass and soil; or (iii) bottom-up modelling of ecophysiological processes from chamber measurements (leaves, stems, roots and soil). Such a consistency assessment requires that all NECB components are estimated during the same time intervals [24].

The components of the NECB are in practice directly measured by the eddy-covariance (EC) technique or derived from such measurements [25], which is to date the state-of-the-art for obtaining ecosystem-level flux estimates. However, there are limitations associated with the EC method, namely, being (i) bound to local measurements and (ii) the use of fixed and costly instrumentation. This entails the need to assume that such areas are representative of ecosystem types. However, observational gaps exist, and single ecosystem types may not be sufficiently representative of ecosystem functioning under diverse environmental conditions and management practices. Hence, there is a requirement for improved flexibility of methods. It is in this context that approaches based on mobile platforms have shown to be of help [26, 27, 28, 29].

The main interest in advancing unstaffed aerial vehicle (UAV)-based methods lies in profiting from the flexibility and scalability that mobile platforms provide, thereby gaining independence from restrictions associated to the use of fixed instrumentation. In the last decade, UAV methods employed to monitor fluxes and crop status have provided significant advances. Hoffmann et al. (2016) [26] investigated the potential of UAV imagery-based estimates to provide crop water stress maps in barley fields. Recently, Hollenbeck and Chen (2021) [27] presented a method using multiple UAVs for assessing continuous flows inside a gas emission plume. Also, Hollenbeck et al. (2022) [28] proposed a method for quantifying ecosystem-based fluxes, by flying upwind and downwind the emission source point, and evaluating gradients. The integration of UAV-based data and ecosystem modelling has also been explored: Wang et al. (2020) [29] introduced a method for estimating interpolated land surface fluxes derived from a combination of UAV-based imagery and a dynamic soil-vegetation-atmosphere model. The findings revealed that the UAV-borne imagery proved useful in calibrating soil and vegetation parameters, ultimately achieving validated flux estimates (e.g. GPP) within 13-15% agreement with EC measurements.

In precision agriculture, UAV-based remote sensing is being increasingly applied to assist in above-ground biomass (AGB) and flux assessments due to the ability of UAV-borne sensors to capture the spatial distribution of land surface variables at high spatial resolution and flexible revisit times [30]. Moreover, UAV-based remote sensing has been shown to be a valid means to complement EC measurements for estimating fluxes under cicumstances where data monitoring is limited [29]. To date, the majority of studies use UAV-photogrammetry (e.g. structure-from-motion techniques) to calculate AGB as a function of plant height metrics (e.g. maize [31, 32, 33], corn [34], rice [35], barley [36, 37] cotton [38] , or winter wheat [39, 40]). Yet another line of research aims to assess AGB as a function of vegetation indices using spectrally resolved sensors in different cash and food crops (e.g. spring wheat [41], winter wheat [42, 43, 44], corn and soybean [45], and rice [46]).

More recently, the advent of mobile light detection and ranging sensors (UAV-LiDAR) has not only upgraded the spatial resolution of data sets, but also included the vertical component, creating volumetric data structures (i.e. point clouds). This has allowed to enhance crop phenotyping [47] and map AGB in croplands at a sub-meter resolution [30] by leveraging the structural information of vegetation from 3D point clouds. UAV-LiDAR have provided a workaround to previous obstacles in UAV-based crop phenotyping, namely the spectral saturation in image-based vegetation indexes, especially during maturity of crops.

The motivation of this study is to leverage the capabilities of UAV-LiDAR sensors together with machine learning (ML) regression methods in order to provide estimates of plant C stocks in croplands, thereby contributing to advancing current techniques in ecosystem C budgeting from mobile platforms.

Here, we investigate the degree of agreement of two independent methods— (i) UAV-LiDAR surveying of the temporal development in the C stock and (ii) flux-based EC measurements—in obtaining concurrent estimates of assimilated atmospheric C stocks in a crop field, subject to a cereal crop rotation scheme during two consecutive years. Specifically, we propose and evaluate a method to estimate *in situ* plant C at the plot scale using UAV-LiDAR and a ML-based approach, and compare the results obtained with the respective NPP during identical time intervals.

Results showed that the integration of LiDAR-based estimates to track the temporal growth of C in crops may offer a valuable tool for expanding EC estimates across agricultural landscapes. The contribution of this study to current research in C stocks in croplands lies in the proposal and evaluation of a UAV-LiDAR method to estimate cumulative C fluxes along the crops' growing season.

# = Materials and Methods =

## Study Area

The study area (Figure 2) is a conventionally managed cropland site located around an Integrated Carbon Observation System (ICOS) [48] class-1 ecosystem station at Voulund, (DK-Vng) in Mid-Jutland, Denmark (56.037476N, 9.160709E). Located on the eastern part of the Skjern River catchment, covering an area of ca. 13 ha. The field is a flat plain at an altitude of 64-68 m above mean sea level, with smooth undulations and a slight slope to the northwest. The ploughing layer (30 cm deep) sits on a sandy soil (>99%) with pebble inclusions of ca. 3-5 diameter. The water-table depth lies at 5.5± 1 m below ground. The region presents a humid temperate climate characterized by a mean annual precipitation of 961.0 mm, mean annual temperature of 8.1 °C, and usually overcast or scattered cloud cover (mean annual incoming short-wave radiation of 108 $W/m^2$). For an insightful description of both functional and topographic characteristics of the Voulund agriculural site, the reader is referred to Jensen et al. (2016) [17]

The crops investigated were spring barley (*Hordeum vulgare L.*) and winter wheat (*Triticum aestivum L.*) during 2020 and 2021. The growing period of the barley crops lasted from the end of 04/2020 (seedling emergence) to the end of 08/2020 (harvest), following a similar cycle in the 2021 season. In 2021, the growing period of winter wheat extended from 01/2021 (seedling emergence) until the end of 08/2021 (harvest). The conventional agricultural practice at the site included the application of fertilizers in the form of pig slurry, according to ministerial regulations [49], pesticides and fungicides along the growing season, as well as sufficient irrigation to prevent water stress [17]. This corresponds to a maximum amount of fertilizer of 159 (N) and 21 (P) kg/ha and 202 (N) and 19 (P) kg/ha for spring barley and winter wheat, respectively.

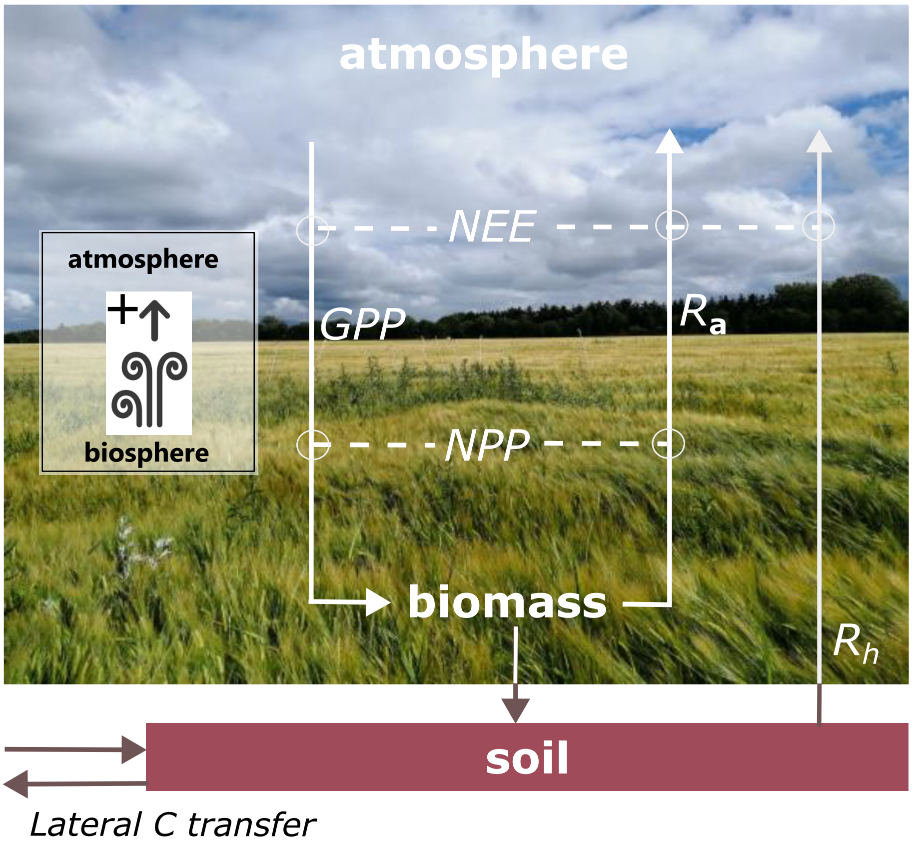


**Figure 1.** Components of the net ecosystem carbon balance (NECB). The inset on the left indicates the sign convention for fluxes calculation. NEE: net ecosystem excange. GPP: gross primary productivity. NPP: net primary productivity. NEE: net ecosystem exchange. $R_a$: autotrophic respiration. $R_h$: heterotrophic soil respiration. Lateral carbon transfer refers to human intervention (e.g. harvest, fertilization).

## UAV-LiDAR Survey and Point Cloud Data

We used a UAV-borne LiDAR system mounted to a DJI Matrice 600 Pro payload at a 90° pitch angle, and same heading and roll as the UAV platform. The system included a discrete infrared LiDAR scanner (M8 sensor, Quanenergy Systems, Inc. Sunyvale, CA, USA) and the corresponding industry standard inertial and navigation systems. In addition, we used a ground based differential Global Positioning System (dGPS, Trimble R8) during the UAV-LiDAR survey, set up in post-positioning kinematic (PPK) mode, which logged real-time satellite coverage (cf. Ravenga et al. 2022 [30] for details on the airborne and ground system). The coupling of the satellite coverage data with the UAV-based laser and navigation data produced allowed the generation of georeferenced point cloud data (PCD) scenes, following Davidson et al. (2019) [50]. We visualized the PCD scenes of barley and wheat crops at maturity stage in Figure 3 (a and b, respectively). It can be noted how the PCD scenes reflect a higher porosity in the crops of 2021, than in 2020. This corresponds to a more sparse canopy structure in the second year than in the first (Figure 5, a.2 and b.2).


**Figure 2.** Location of the study site (⋆) in Mid-Jutland (DK). The inset shows a top-down view of the field site and the surrounding area. Source: www.icos-cp.eu and Google Earth Engine.

UAV-LiDAR data were acquired according to the planned UAV-LiDAR survey at a height of 40 m above ground level. Following a regular auto-pilot flight grid, we ensured a 20% overlap between individual LiDAR scans of ca. 50 m width and 250 pp/$m^2$ (cf. Revenga et al. 2022 [30] for additonal details on applied flight parameters). The surveys were conducted during May-July 2020, and during April-July 2021, coinciding with the two growing seasons.

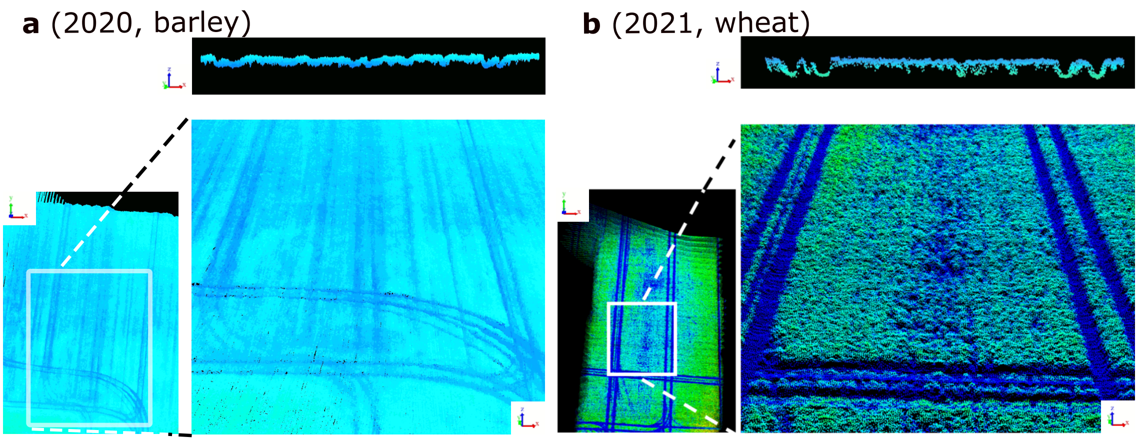


**Figure 3.** Point cloud data (PCD) scenes. The crops are portrayed at maturity stage. **a**: barley field, during 2020. **b**: wheat field, during 2021. The PCD scenes are colored by elevation. In both **a** and **b**, the upper panes show the cross section view of the PCD, with a buffer depth of 0.5 m. Axes $x$, $y$, and $z$, indicate easting, northing, and elevation, respectively. It can be noted a higher PCD porosity in **b**, than in **a**, corresponding to more sparse crops and lower AGB values.

### Field Based Destructive Measurements of Above-ground Carbon

In order to acquire reference values of biomass (i.e. ground-truth labels) to provide supervision to the ML regression algorithms, samples of AGB were systematically collected from the field at random locations during the growing season (locations shown in Figure 4 and resulting data sets, size and dimensions, are described in Table 1). The AGB sampling procedure followed the ICOS protocol for ancillary vegetation measurements [51] in 2020. During 2021, this AGB sampling procedure was modified, in order to maximize data sample size and quality, with a limited fieldwork capacity. Therefore, in 2021, at each location, three adjacent individual samples were collected. In total, three separate data sets of AGB were produced (Table 1).

An additional AGB dataset in 2021 was produced, composed of *augmented* samples. The augmentation procedure consisted of adding adjacent AGB samples, and their corresponding UAV-LiDAR data samples, so that both the AGB label and the LiDAR counterparts could be recalculated from the resulting combined sample. This augmetation scheme is shown in Figure 4 (c). This procedure allowed to produce one larger dataset (specifically, with 4/3 times more data samples) at a spatial resolution of 0.35-0.52 $m^2$ (cf. Revenga et al. 2022 [30] for a detailed explanation of the augmentation procedure).

We considered the plant carbon content in two separate parts: (i) above-ground and (ii) root carbon components (AGC and $root_C$, respectively). AGB was harvested and measured at randomized locations within the study site, according to ICOS protocols [51], throughout the two growing seasons (Figure 4 shows the sampling locations of AGB). Then, the AGB samples were oven-dried for 72h at 65°, to assess the dry biomass weight. The carbon content associated was measured by a laboratory appointed by the ICOS Ecosystem Thematic Center (ICOS ETC). The plant C content was evaluated as the C-to AGB ratio measured at 16 specific locations from the leaf tissue, where 45 g of tissue from the uppermost and middle-height leaves at each location were sampled. In this way, the C to-AGB ratio was determined as 46.6 ± 0.3% in spring barley, and 47.7 ± 0.3% in winter wheat.

The resulting reference AGC values were resampled to 1 $m^2$ resolution. In such way, we obtained a distribution of surface-based ground-truth estimates of AGC density at a spatial resolution of 1 $m^2$. Table 1 provides a comprehensive overview of the sample count and spatial dimensions AGC reference labels in this study. The spatial distribution of the AGC sampling points is visualized in Figure 4 (b).

**Table 1.** Description of above-ground carbon (AGC) data sets. The subindex *aug.*, refers to the *augmented* dataset.

| Growing season | Data set name | Number of samples | Sample dimensions (m) |
|---|---|---|---|
| 2020 | $barley_{20}$ | 104 | 1 x 0.35 |
| 2021 | $wheat_{21}$ | 455 | 0.5 x 0.35 |
| | $wheat_{21,aug.}$ | 609 | (1-1.5) x 0.35 |

Additionally, we considered the amount of photoassimilated C not stocked as plant biomass or respired back into the atmosphere, but translocated to the soil as rhizodeposits (i.e. $soil_C$). We relied on existing literature to estimate the C content translocated into the soil. In conventionally managed crop fields, $soil_C$ in sandy soils has been previously measured using $^{14}$C labelling and reported as a relative fraction of GPP. Paush and Kuzyakov (2018) [52] report of a mean value of 1.4% across 281 datasets including different crops and grasslands, while species-specific studies report of 4-9% [53] and 2.2-2.9% [54] for wheat, and 0.4-2.4% [55] for barley.

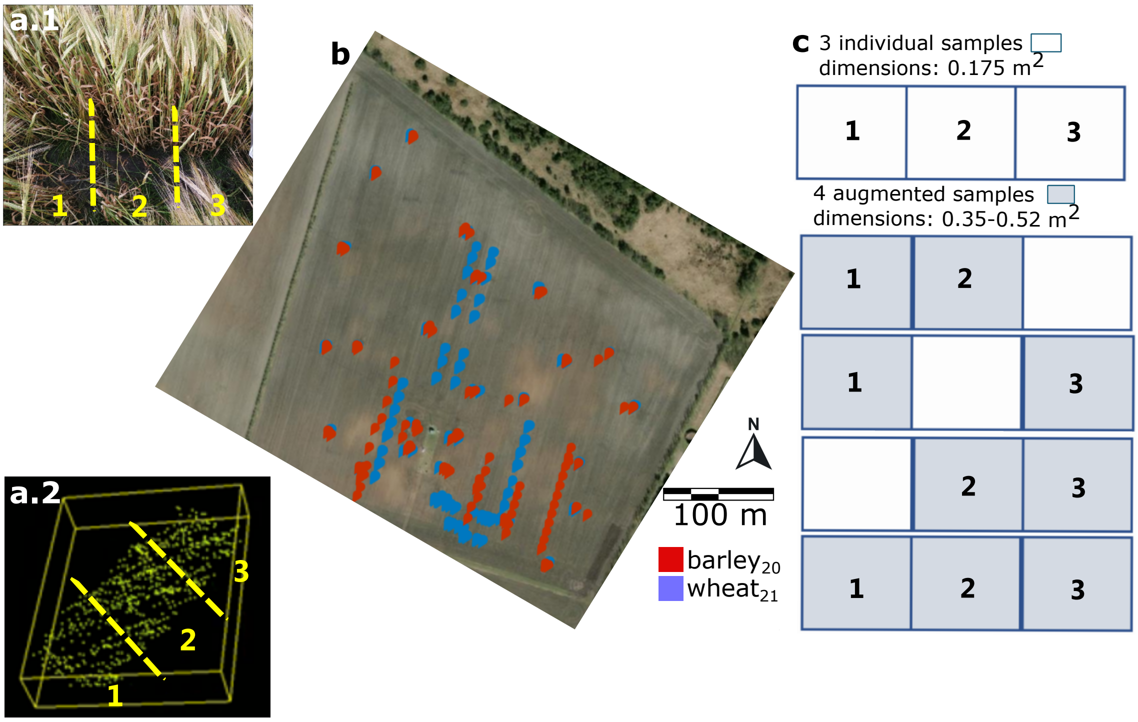


**Figure 4.** **a.1**: Three adjacent above-ground biomass samples (AGB) and the corresponding three LiDAR samples (**a.2**, dimensions of each sample: 0.5 × 0.35 m). **b**: The spatial distribution of the AGB sampling locations. Each color indicates one of the original data sets: **red**: barley samples collected in 2020 (i.e. $barley_{20}$); **blue**: wheat samples collected in 2021 (i.e. $wheat_{21}$). **c**: dimensions of three original AGB samples (above), and data augmentation scheme by permutation (below); i.e. adding either two or three samples).

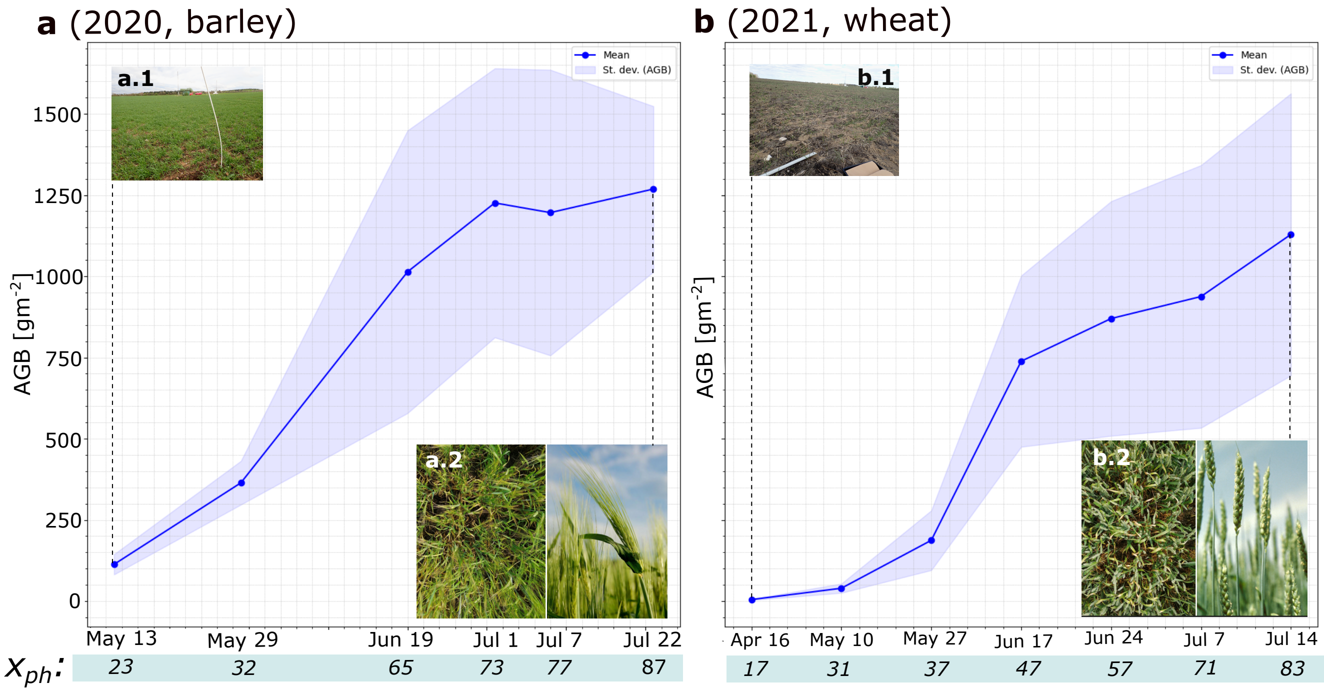


**Figure 5.** Crop development along the two growing seasons considered. Above-ground biomass (AGB) development during 2020 (**a**, barley) and during 2021 (**b**, wheat) growing seasons, respectively, indicating the dates of AGB sampling events. Y-axis indicates dry AGB matter. The blue solid line indicates the mean per sampling campaign, while the shaded area covers ± the standard deviation. **a.1, a.2:** spring barley crop structure at the start of the sampling campaign and at maturity stage, respectively. $x_{ph}$: phenological growth stage (Zadoks decimal code) [56]. **b.1, b.2:** winter wheat crop structure at the start of the sampling campaign and at maturity stage, respectively. The AGB sampling during 2021 started earlier than in 2020, hence an initial value close to 0 at the start of the 2021 season.

## Flux calculation

The study site is equipped with an eddy covariance (EC) system constituted of Gill HS-50 sonic anemometers (Gill Instruments Ltd, Lymingdon, UK) and LI-7200RS enclosed infrared $CO_2/H_2O$ gas analyzers (LI-COR, Lincoln, NE, USA) sampling at a frequency of 20Hz. The station is further equipped for air- and soil-meteorological monitoring (air temperature: TA, relative humidity: RH, air pressure: PA, global radiation, Rg, PPFD: photosynthesis active photon flux density, soil temperature: TS, soil water content, SWC) with state-of-the-art instrumentation complying with ICOS protocols for a class 1 ecosystem station [48].

### *Raw data processing*

Raw 20 Hz wind, $CO_2$, water vapor, and sonic temperature data were processed utilizing the EddyPro v. 7.0.9 software (LI-COR, Lincoln, NE). Half-hourly turbulent scalar fluxes were calculated as the covariance between vertical wind speed and scalar variables (i.e. $CO_2$, $H_2O$, T). The processing included statistical tests for raw data screening [57], double coordinate rotation, block averaging, time-lag optimization to maximize covariance, compensation for the effect of density fluctuations on fluxes [58, 59], and low- and high-frequency spectral correction [60]. Half-hourly turbulent scalar fluxes were calculated as the covariance between vertical wind speed and scalar variables (i.e. $CO_2$, $H_2O$, T). The raw data processing, quality control, and subsequent gap-filling procedures approximated the standards applied by ICOS ETC [48, 61]. The EC data produced at DK-Vng became part of the ICOS ETC database only in 2021. Therefore, in order to apply the same treatment to the two datasets (i.e. 2020 and 2021), we processed the raw data according to the ICOS ETC standards.

### *Post-processing: Spike Removal, Quality Control, and Gap Filling*

During raw data processing and post-processing, low quality data were rejected leaving gaps in the dataset. This data screening consists of two sub-tasks: (i) an absolute limit test, that sets boundaries for a physically plausible range of values, and (ii) individual outliers were detected following the method proposed by Papale et al. (2006) [62]. Additionally, data were removed when the wind came from the direction of the instrumental plot (Figure 6, b).

During 2020's growing season, this resulted in a 56.8% of data rejected after all three filtering tests were applied. While the gaps occurred mainly at the beginning and end of the 2020 year (Autumn and Winter), the growing season was better populated with valid NEE data values. The data were gap-filled according the method proposed by Reichstein et al. (2005) [63], and the u*-filtering procedure was based on season.

The processing of the 2021 flux data set followed the same procedure as for the 2020 season. The processed data showed a missing ratio of 32.9% after the quality control test and de-spiking, showing fewer gaps than the previous year and also a better flux data recording during the growing season.

To acquire a continuous dataset and allow to estimate *in situ* carbon budgets, data gaps were filled following the method of Reichstein et al. (2005) [63], using the REddyProcWeb tool. The method combines lookup tables of average fluxes under comparable meteorological conditions in a certain time window. If meteorological measurements are also missing, fluxes are estimated as the mean flux at the same time of the day in each time window (i.e. mean diurnal course).

### *Estimation of Flux Climatology Footprint*

We calculated the flux climatology footprint using the model developed by Kljun et al. (2002) [64], and extracted the polygon covering the 70 % influence around the station (Figure 6, **a**).

In order to remove the influence of the instrumental plot surrounding the EC tower on the measurements, this area was masked out. For the 2020 dataset, the wind directions that covered the instrumental plot (18–198°) were excluded of further processing. The wind directions excluded in 2021 (18–116°) differed from the previous year due to a change in size of the instrumental plot. For this reason, in Figure 7, AGC maps show different shapes in each year.

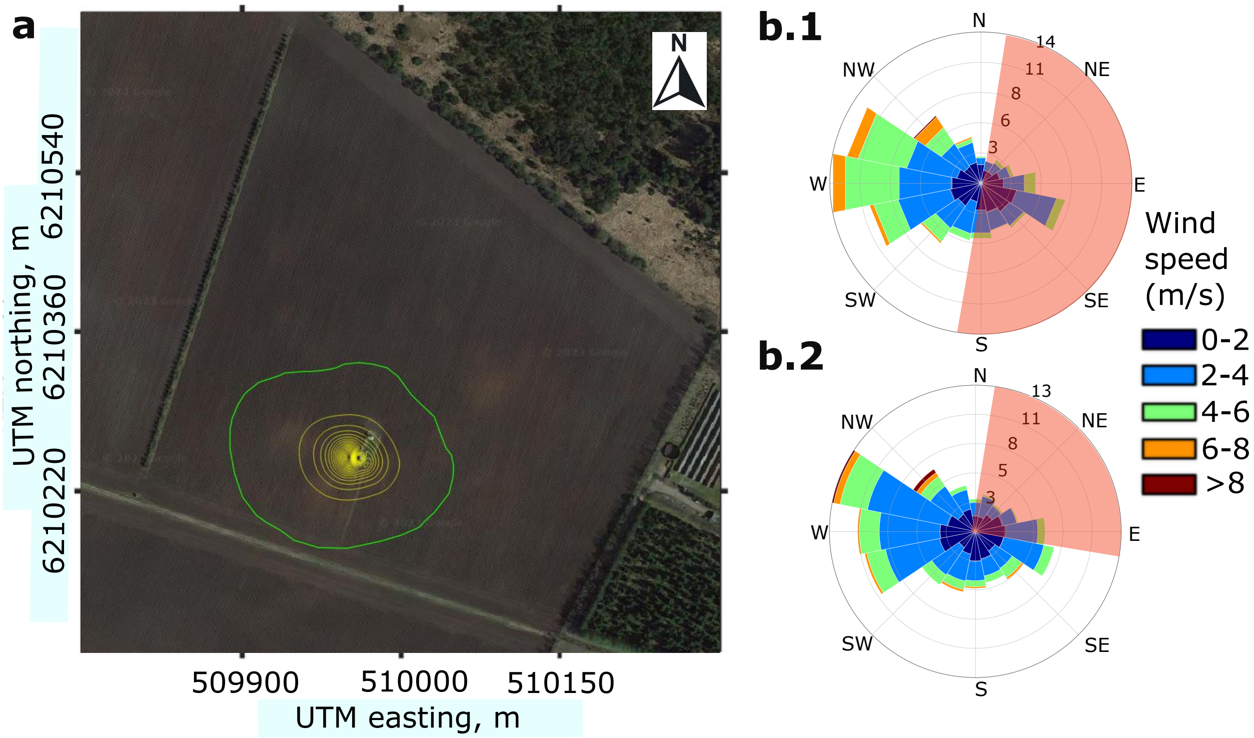


**Figure 6.** **a:** Flux footprint climatology map from the study site; the yellow contours indicate areas of 10 % increase of influence (source of background image: Google Earth 2023). **b.1, b.2:** wind frequencies at the study site during April–August of 2020 and 2021, respectively. The radius indicates total frequency of a given wind direction; the color indicates wind speed ($ms^{-1}$). The shaded red areas cover the wind directions influenced by the instrumental plot—that were filtered out for flux analysis.

### *Ecosystem Flux Balance*

After data processing, the flux data sets provide an estimate of the net ecosystem exchange (NEE) (Figure 11, Appendix), allowing to estimate other NECB components. The estimation of net primary productivity (NPP) involved calculating the difference between NEE and ecosystem respiration. Therefore, we considered the flux balance

$$NPP = (-NEE) + R_h \tag{1}$$

where $R_h$ accounts for the heterotrophic respiration, while $R_a$ (i.e. autotrophic plant respiration is contained within NPP. As per the usual convention, the negative sign indicates flux direction towards the ecosystem; the positive sign indicates a flux release towards the open atmosphere.

In conventional croplands (Figure 1), where the influence of higher-order heterotrophs (e.g. mammals, birds) can be considered negligible, the microbial soil respiration ($R_{soil}$) constitutes $R_h$. Here, we modelled $R_{soil}$ as a function of soil temperature during winter. Following Lloyd and Taylor (1994) [65], a second-order polynomial was fitted to the measurements of NEE prior to the start of the growing season (i.e. constituted of the $R_h$ component only), as function of soil temperature 5 cm below surface. We filtered out $R_{soil}$ values corresponding to frozen conditions (i.e. $< 0.5$ °C) for the model fit. Then, we extrapolated the modeled $R_{soil}$ to the entire growing season. In 2020, as many datapoints were missing for $T_{soil}$, we filled the gaps with $T_{air}$, introducing a higher amplitude in the recorded values (therefore, also some added uncertainty in the estimate of NPP values).

### Machine Learning-based Carbon Estimates

#### *Training, Evaluation and Validation of Predictions*

Three different ML regression models were initially selected for the task of AGC prediction. They were calibrated on a training dataset, and their performances were evaluated on a separate validation dataset; then, the best performing one was chosen for testing. This procedure helped avoid overfitting the model to the data, preventing an optimistically-biased accuracy assessment.

Therefore, we selected three fundamentally different ML methods; one representative of regularized linear models (i.e. Huber regressor [66, 67]), one tree-based ensemble method (i.e. Extreme Randomized Trees [68], ERT), and one exemplar from the boosting methods (i.e. Extreme Gradient Boosting [69]).

The model performance on the validation set was assessed via the average performance (indicated by the overbar) of the following metrics over ten randomized executions: coefficient of determination ($\overline{R^2}$), mean squared error ($\overline{MSE}$), mean absolute percentage error ($\overline{MAPE}$), and mean absolute error ($\overline{MAE}$). ERT obtained the best results across all four scores and therefore was selected as the model of choice. For more details on the model selection, validation and test procedure cf. Revenga et al. (2022) [30].

#### *Description of the Model Selected*

Extremely Randomized Trees (ERT) is an ensemble learning technique that aggregates the results of multiple individually created decision trees to output regression results [68]. It is originally derived from the Random Forest (RF) model [70]. In an ERT model, every individual predictor—i.e. a binary decision tree—of an ERT is constructed from the whole training set. A single tree decides at each node, which split of a random subset of features splits reduces the reconstruction error (e.g. MAE or MSE) the most. The random sampling of features and the random splits within the features range leads to more diverse and thus less correlated decision trees, thereby leading to impoved generalization results. Each tree is considered to be a "weak" regressor performance-wise but the combination creates an ensemble that outperforms the individual regressors. As final prediction, the average predictions of the individual decision trees in the forest is used, providing an estimate of above ground carbon (i.e. $\widehat{AGC}$).

### Above-Ground and Root Carbon Estimates

Using the AGB prediction results (Figure 7), and the C-to-biomass ratio measured, we calculated the total AGC within each EC footprint. Then, the total plant C estimates were obtained by calculating at each point the total plant C derived from the AGC prediction. In order to obtain this estimate, we considered the allocation of C below ground as a function of the phenological stage using Eq. 2 (Figure 8), fixing $root_C$ at anthesis as $10 \pm 1\%$ of total plant C at maturity of crops, according to reference literature [71]. Therefore, $root_C$ was calculated as a function of

(i) AGC, (ii) the rate at which GPP is translocated to the roots ($GPP_{roots}$) [72], and (iii) the phenological stage (i.e. $x_{ph}$) [56]:

$$root_C(x_{ph}) = \begin{cases} x_{ph} \cdot GPP_{roots}, & \text{if } x_{ph} < x_{anthesis} \\ (0.1 \pm 0.01) \cdot AGC_{mat}, & \text{if } x_{ph} = x_{anthesis} \\ root_{C,post}(x_{ph}), & \text{if } x_{ph} \geq x_{anthesis} \end{cases} \tag{2}$$

where $AGC_{mat}$ indicates above-ground carbon at maturity stage; the function $root_{C,post}(x_{ph})$ was defined by a linear fit to $root_C$ at anthesis and values of $GPP_{roots}$ in literature at each growth stage, for wheat and barley in sandy soils, respectively [72]. Similarly, $GPP_{roots}$ was obtained as the slope of a linear fit between the onset of the season and $root_C$ at anthesis.

Likewise, $soil_C$ at each date was calculated as a linear fit to the values reported in literature of $^{14}C$ pulse-labelling for barley [54] and wheat [73] in sandy soils. This resulted on an average translocation of GPP to rhizodeposits of 2.73% and 1% for barley and wheat, respectively.

# = Results =

## Plant Carbon Maps

We selected nine UAV-LiDAR survey dates (five during 2020; four during 2021), and intersected them with the 70 % of the area of influence surrounding the eddy-covariance station. For each UAV-LiDAR survey in 2020 and 2021, we created a map of AGC at 1m$^2$ spatial resolution (following the procedure described in Revenga et al., 2022 [30]).

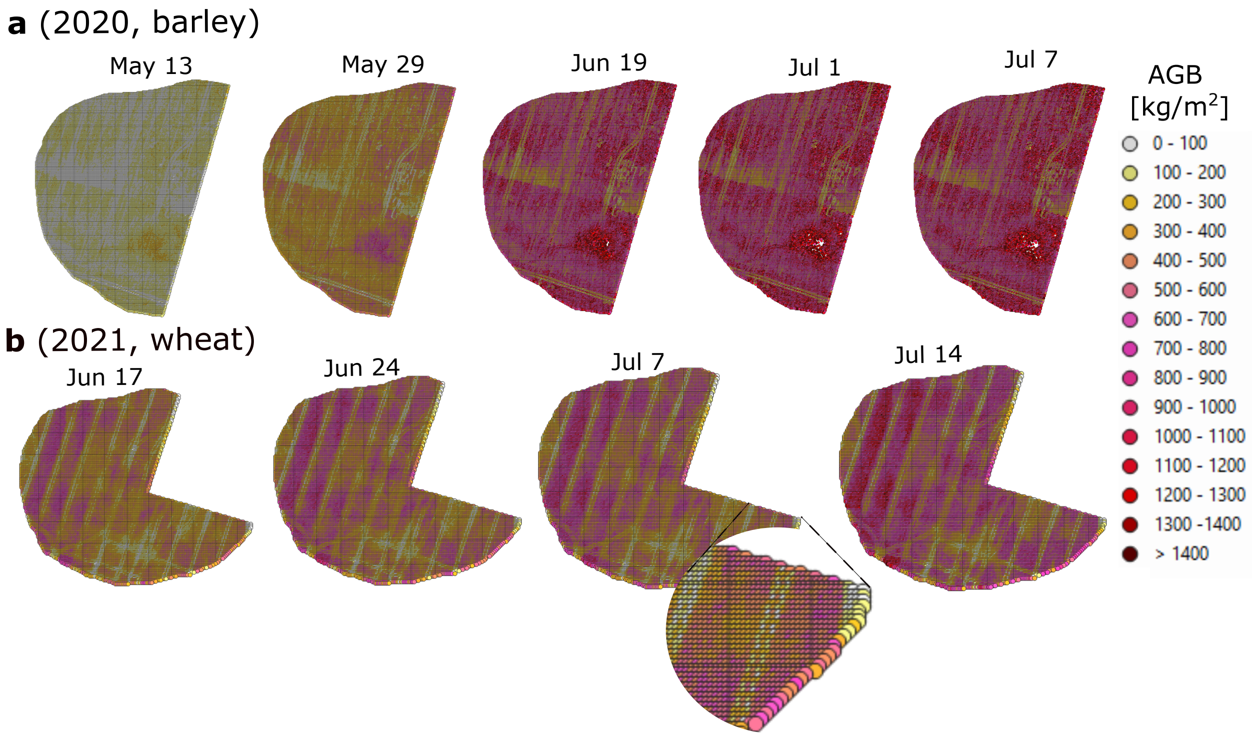


**Figure 7.** Exemplary above-ground biomass (AGB) maps. **a:** 2020 growing season; **b:** 2021 growing season. Values in legend indicate predictions of dry AGB matter. A sector of the eddy-covariance station footprint was clipped out to avoid influence from the instrumental plot on the results: in 2020, the (18–198)° wind directions were excluded; in 2021, the wind directions (18–116)° were excluded.

## *Above- and Below-Ground Carbon Estimates*

In 2020, the AGB collection campaign started at a level of 100 $gm^{-2}$ of AGB. In Figure 5 (**a**) it can be observed a steady linear increase until 1 July, where there is a turning point, and a saturation plateau afterwards. From then onward, AGB stabilizes, i.e. by the harvesting date (end of July), the AGB are just slightly above the one measured on 1 July.

In contrast, in order to extend the span of AGB measurements, during the 2021 campaign the AGB sampling started at a point slightly above 0 $gm^{-2}$, where can be noted a slow start of AGB accumulation. By approximately the same date (27 May), the AGB in 2021 growing season lags 150 $gm^{-2}$ behind the previous year. This can be compared with the NEE of both years (Figure 11, in Annex) showing a "false start" in 2021 11 (b), so until start of June NPP barely offsets $R_{eco}$. Instead of saturating by 1 July, AGB kept growing until the last sampling date. This observation was expected, considering that the crops in 2021 exhibited a time-lag of approximately 15 days compared to the previous year (see Figures 11 and 12, in Annex).

The difference in AGB between the two years translates linearly to differences in AGC by modeling C content to be constant across all plant tissue ($46.6 \pm 0.3\%$ in barley, and $47.7 \pm 0.3\%$ in wheat). Notably, wheat moves a greater amount of photoassimilated C below ground compared to barley, in relative terms. This different strategy becomes increasingly evident as the growing season progresses and becomes particularly apparent at the maturity stage.

The difference between the measured AGC in both growing seasons (i.e. $\approx 235$ g$m^{-2}$ more in 2020 than in 2021) can be attributed to the harsher environmental conditions that the 2021 crops endured at the beginning of the season, causing a delay and a sparser structure (Appendix).

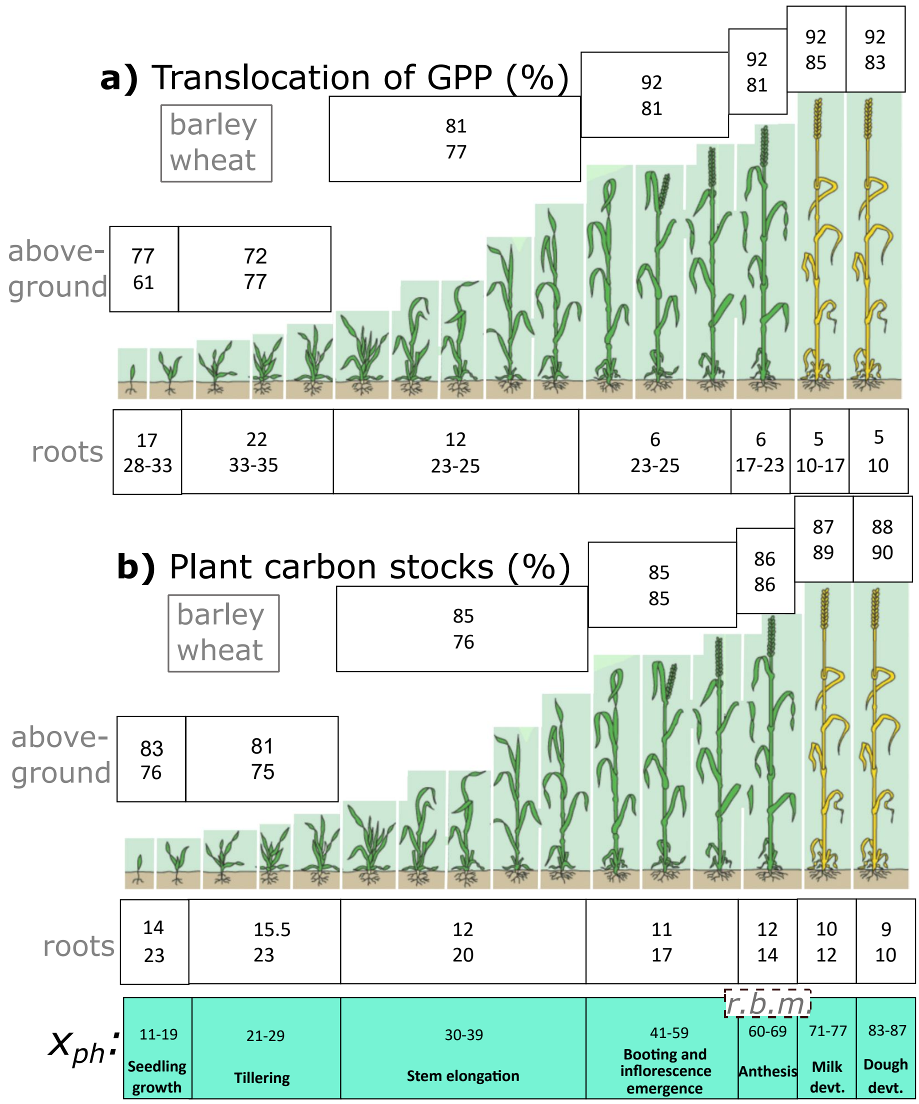


**Figure 8.** **a:** Translocation of photoassimilated atmospheric carbon (i.e. GPP) to above-ground and root components (rhizodeposits are not included); values in white boxes indicate estimated % corresponding to the same phase. **b:** Plant carbon stocks along the growing season showing the estimated carbon allocation at each phenological stage (adapted from [74]). Percentage values of carbon in roots (both translocated and stocks) are derived from [72] for wheat and barley crops in sandy soils. Each white box shows values for spring barley (above) and winter wheat (below). $x_{ph}$: phenological growth stage (Zadoks decimal code) [56]. The inset indicating r.b.m. shows the stage when the root biomass maximum occurs.

### Carbon fluxes from the eddy-covariance method

The cumulative NPP curves of the two growing seasons considered are shown in Figure 9. the progression of the curve in the year 2020 exhibits saturation by the terminal data collection (i.e. on July 22), whereas in the subsequent year, 2021, the ultimate survey (i.e. July 14) coincides with a phase characterized by the ongoing ascendant trajectory of the net ecosystem's uptake.

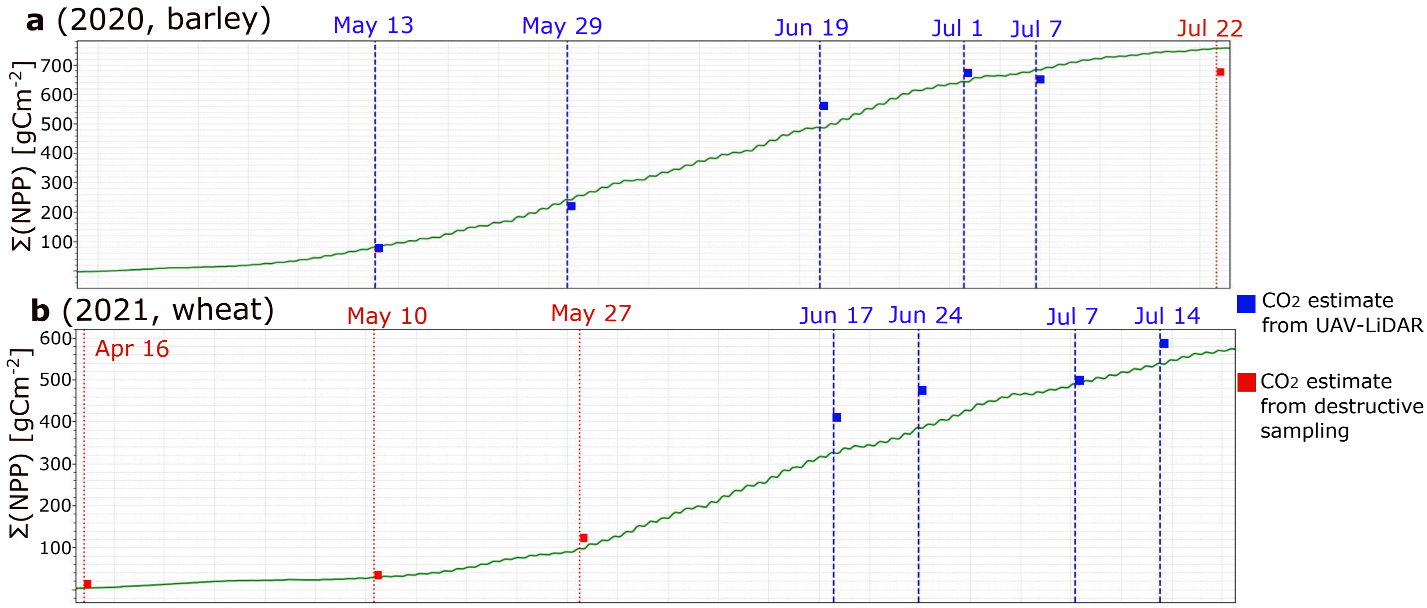


**Figure 9.** Cumulative NPP (gCm$^{-2}$) along (**a**) the 2020 and (**b**) the 2021 growing seasons. The red dotted vertical lines indicate above-ground biomass (AGB) sampling dates, while the blue dashed lines indicate dates in which both AGB sampling and UAV-LiDAR surveys took place. The square marks indicate the plant-C estimates for a given date using the UAV-LiDAR method (blue dates), or based on C estimated from destructive sampling (red dates).

## Comparing Flux Data and UAV-based Plant Carbon Estimates

Table 2 shows the results of the plant carbon estimates via the UAV-LiDAR method against the cumulative partitioned fluxes estimated via the eddy-covariance method.

In order to quantify the degree of over- or underestimation that the UAV-LiDAR-based method produces with respect to the cumulative NPP, we used the following metric, referred to as delta-ratio ($\Delta_C$). It is defined as the ratio between the increment of plant C and the increment in NPP between two separate surveying dates:

$$\Delta_C = \frac{\Delta(NPP_{i,j}) - \Delta(PlantC_{i,j})}{\Delta(NPP_{i,j})} \cdot 100 \tag{3}$$

where the subindexes $i, j$ refer to two different surveying dates.

**Table 2.** Results of carbon estimates via te two independent methods considered. The first column indicates the UAV-LiDAR survey dates; second and third columns show the plant carbon stock estimated via the UAV-LiDAR method (both AGC and $root_C$); the last three columns show the cumulative values (from the start of the photosynthetic season) of the ecosystem flux components partitioned into net ecosystem exchange (NEE), heterotrophic respiration $R_h$ and net primary productivity (NPP). $x_{ph}$ indicates the average phenological growth stage (Zadoks decimal code) [56] measured at 12 control plots. $soil_C$: rhizodeposits.

| **Method** | | **UAV-LiDAR** | | | **Eddy-covariance** | | |
|---|---|---|---|---|---|---|---|
| d/m/yyyy | $x_{ph}$ | **AGC** $[gm^{-2}]$ | **root**$_C$ $[gm^{-2}]$ | **soil**$_C$ | **-NEE** $[gCm^{-2}]$ | **R**$_h$ $[gCm^{-2}]$ | **NPP** $[gCm^{-2}]$ |
| 13/5/2020 | 23 | 52.4 | 8.9 | 1.72 | 35.7 | 143.4 | 91.0 |
| 29/5/2020 | 32 | 168.8 | 32.0 | 5.63 | 81.9 | 237.9 | 252.5 |
| 19/6/2020 | 65 | 469.3 | 65.2 | 15.0 | 286.1 | 423.0 | 497.7 |
| 1/7/2020 | 73 | 567.5 | 75.1 | 18.0 | 401.4 | 533.1 | 653.8 |
| 7/7/2020 | 77 | 553.6 | 66.4 | 17.4 | 423.6 | 577.7 | 693.7 |
| 22/7/2020 | 87 | 587.3 | 58.7 | 18.1 | 463.4 | 681.8 | 767.6 |
| 16/4/2021 | 17 | 2.3 | 0.7 | 0.0 | 83.6 | 90.7 | 0.9 |
| 10/5/2021 | 31 | 18.4 | 5.5 | 0.3 | 147.6 | 100.8 | 25.5 |
| 27/5/2021 | 37 | 86.7 | 25.8 | 1.1 | 68.6 | 229.5 | 94.5 |
| 17/6/2021 | 47 | 341.9 | 55.5 | 4.0 | 102.5 | 418.4 | 321.3 |
| 24/6/2021 | 57 | 402.7 | 58.0 | 4.7 | 144.3 | 482.0 | 372.5 |
| 07/7/2021 | 71 | 434.1 | 50 | 4.9 | 227.3 | 592.1 | 486.1 |
| 14/7/2021 | 77 | 522.6 | 48.5 | 5.8 | 251.5 | 672.1 | 532.0 |

## = Discussion =

This study presents a comparison of two independent methods to estimate C uptake in managed croplands. We assessed a method that utilizes UAV-LiDAR technology to derive C dynamics in croplands by surveying the ecosystem along two growing seasons, covered by barley (in 2020) and wheat (in 2021). The results obtained compare favorably with respect to the cumulative NPP when the first UAV-LiDAR survey date is taken early in the growing season; conversely, comparisons lose consistency when time intervals between surveying dates are short, concurrently with a late phenological stage.

### Plant Carbon Components: Values and Uncertainty

The uncertainty estimate of the AGC component was derived from the AGB sampling technique, because, assuming a constant ratio of AGB:C, the uncertainty on the lab analysis (i.e. $\pm$ 1% of C-to-AGB ratio) is comparatively negligible with respect to the AGB uncertainty (i.e. AGB label noise). While certain studies report of uneven C-to-AGB ratios along the plant components—specially seeds and grain-bearing organs—[..], we assumed this ratio to stay relatively constant across the plant components. We consider AGC as the component most accurately assessed between the above- and below-ground components.

Management practices and environmental factors affect the BGB-to-AGB allometric ratio in cereal crops (e.g. root depth is function of soil moisture content) [...], therefore such BGB estimates are usually prone to bias or uncertain [71]. $root_C$ is much depending on availability of water,

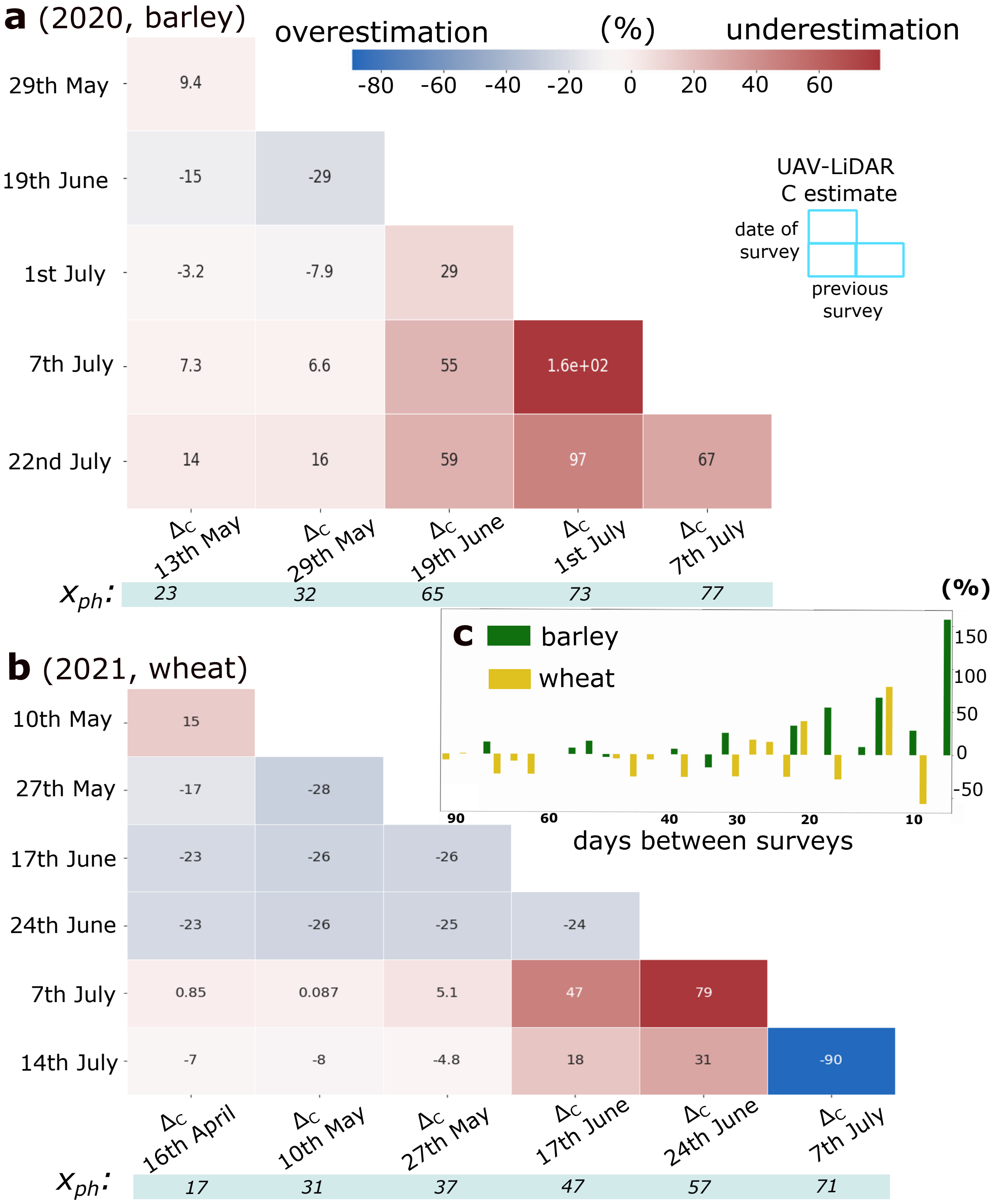


**Figure 10.** Carbon delta-ratio ($\Delta_C$) values between pairs of surveying dates during the 2020 **(a)** and 2021 **(b)** growing seasons; the reference ($\Delta_C = 0$) is the cumulative NPP at a given date. The inset **(c)** shows the error distribution along the time between UAV-LiDAR survey dates for both crop types. It can be noted that (i) LiDAR estimates become more in agreement with NPP as time between surveys increases, and that (ii) considerable over- and underestimates are found between closely spaced dates during a late phenological stage (right tails of both **a** and **b** tables). $x_{ph}$ indicates the average phenological growth stage.

nutrients and nonstructural carbohydrates [...]. Moreover, there is high variability in $root_C$ along the growing season, increasing towards the flowering period (i.e. anthesis), and then gradually decreasing towards maturity ([72]), as nutrients are dynamically allocated to the upper parts during the last crop development, sourcing from the roots. Here, following Hu et al. (2018) [71], we estimated the BGB at anthesis (which corresponds to the root biomass maximum in Figure 8), as given by the ratio $\frac{root_C}{(AGC+root_C)} = 0.10 \pm 0.01$. This ratio relates AGC (at maturity) and $root_C$ (at anthesis, standardized to 25 cm depth). It holds for conventional farming systems and is also supported by findings of Chiranda et al. (2012) [75]. The phenological growth stage [51] indicating anthesis (Zadok's decimal code of plant development = 65) [56] was observed on 18 June 2020. In 2021, the anthesis stage was not recorded, but based on field image documentation, was estimated to correspond to 1 July 2021. Following this ratio, and the rate of photoassimilated C translocated to roots for barley and wheat in sandy soils [72], we estimated the $root_C$ component at each biomass sampling date. We acknowledge that variations in season-specific environmental conditions can lead to differences in such ratios [..]. Therefore, one of the limitations of our method lays on the fact that we estimate per-component C stocks as if they in fact distribute C as reported in the existing literature for the same crops under similar conditions.

Provided that the Hu's ratio [71] is robust and applicable to the environmental conditions of our study, the results presented in this study are therefore most limited with respect to the design of the AGC sampling campaigns for each individual date.

Our sampling design was conceived to optimize predictability of AGC from the PCD data, however, our sampling design turned out to be suboptimal for the application of comparing entire plant C and flux-based estimates on individual dates. Ideally, for the task of intercomparison of C stocks, at every date the locations for AGC sampling should be entirely randomized, across an area which is (i) large enough, and (ii) either within the flux tower footprint or representative of the vegetation traits contained within the footprint.

However, in specific dates, it was found to be advantageous for predicting *in situ* AGC to collect data from locations with contrasting AGB values. This approach allowed us to capture the two-dimensional variability of AGC corresponding to the observed variations in the PCD scene. While this procedure facilitates the establishment of an empirical relationship between covariates (i.e. height metrics derived from PCD) and the response variable (i.e. AGC), it compromises the comparability of cumulative fluxes on particular dates. Consequently, it may lead to apparent over- or underestimation of plant carbon stocks derived from UAV-LiDAR data in relation to net primary productivity (NPP). In both years, this is particularly evident in the comparison of $\Delta_C$ stocks when the 7th of July is involved (Figure 10).

From Table 2, it can be observed how, on 7 July 2020, the AGC sample is 14 g lighter than the previous survey date (i.e. 1 July), while the cumulative NPP for the corresponding time period exhibits an increase of approximately 40 g. This corresponds to a decreasing LiDAR-derived plant-C estimate between these two dates (Figure 9, a). This disagreement can only be attributed to the inherent bias introduced by the sampling procedure, thereby highlighting the significant impact of the sampling design on the resulting outcome. Ideally, during each AGB sampling date, data collection should be completely randomized, without intervening explicitly to ensure AGC variability.

On certain dates, the presence of sample selection bias [76, 77] introduced by the aforementioned approach resulted in inconsistency when comparing plant C values with flux-based cumulative carbon estimates. This is a reasonable outcome, as the continuous flux-based carbon estimates are unaffected by the AGC sampling design.

**Ecosystem Carbon-Uptake Derived from Flux Data**

A limitation of our approach rests on the fact that $R_h$ was modeled as function of soil temperature, taking as sample data to model $R_{soil}(T_{soil})$ the dates prior to the onset of the photosynthetic season (i.e. December–February). During these dates, temperatures did not span a wide range. Therefore, the low dynamics in the values of soil temperature during the beginning of the year may lead to underestimations in the modeled $R_h$. Accurately modeling heterotrophic soil respiration ($R_h$) as a function of temperature may be challenging, particularly when the range of temperatures before shoot emergence (i.e. onset of photosythetic season) is narrow. This can lead to uncertaities in the predicted values of $R_h$. In order to narrow it down, further studies should consider combining the setup we employed with flux chambers.

The exact dates of fertilizer deposition by the farmer remain unknown. The effect of such field managemet (e.g. fertilizer application, irrigation) cannot be reflected i nhe LiDAR derived C estimates, but do have an impact on the measured fluxes.

**Comparing Flux Data and UAV-based Plant Carbon Estimates**

Figure 10 shows the result of the comparison of C stocks obtained via the two independent methods, as delta values ($\Delta_C$). Several observations can be made:

- (i) The optimal reference date for comparing an increase of plant C stocks is the first date, at the beginning of the growing season. This observation applies to both years.
  - When the $1^{st}$ date is the reference, the mean error of predictions in 2020 shows: 2.5 ± 10.4 % while in 2021 the mean error is -9.0 ± 13.3 %.
  - When taking as reference the $2^{nd}$ date, in 2020 the match between both independent estimates shows a mean error of -3 ± 16.9 %. Likewise, in 2021 the mean error is: -8.9 ± 11.4 %.
  - When considering the $3^{rd}$ date as the reference, the findings indicate a persistent underestimation of 47.6 ± 13.3 % in 2020, whereas the results for 2021 exhibit a closer approximation to the reference NPP value, with a deviation of -12.7 ± 13.3 %.
- (ii) The right tail ends of both tables show that comparing close dates at a late phenological stage results in evident over- and underestimations. So, in addition to the temporal proximity of survey dates, the phenological stage of the crops appears to exert a significant influence.
- (iii) The included inset panel (c) presents the $\Delta_C$ values of both crops, along the temporal interval between survey dates. A clear trend can be observed, indicating a consistent increase in errors as the UAV-LiDAR survey dates approximate.

Figure 12 (in Appendix) shows the cumulative values of $R_{eco}$, NPP, and GPP, in both growing seasons. It can be observed how the C uptake does not offset respiratory ecosystem losses until the $4^{th}$ of June. This represents a time shift with respect to 2020 of 15 days, where the crossing of GPP and $R_{eco}$ occurred in $19^{th}$ of May. This seemingly time lag during the initial stages of the growing season appears to have manifested as a significant temporal displacement of the entire crop phenological process, estimated to be approximately of 15 days. This temporal shift can be visualized by comparing the time discrepancy in the emergence of the uplifting point in NPP between panels a and b in Figure 9.

UAV-based remote sensing is being increasingly applied to assist in ecosystem fluxes analysis due to the ability of UAV-borne sensors to capture changing land surface variables as well as their spatial distribution [29]. The combination of EC towers with UAV-based remote sensing shows potential for estimating ecosystem fluxes in areas where observational gaps exists, due to lack of monitoring capacity or difficult accessibility. Moreover, there is an interest in developing independent methods to estimate the same ecosystem variable (i.e. NECB), in order to target sources of uncertainty, and advance existing techniques.

In this study, the observed disparities between the two methods considered improve the uncertainty reported in previous studies between modeled and empirical approaches to estimate C stocks in croplands. For instance, a 18% of discrepancy between modeled and observed crop mass is reported by Soltani et al. (2012) [78]. However, we consider that the most noteworthy aspect of the proposed method is its ability to provide flexible estimates of carbon fluxes that align well with the EC flux estimates. Furthermore, these estimates can be obtained without reliance on ground-based instrumentation, enabling the assessment of ecosystems that are otherwise inaccessible or poorly documented.

## = Conclusions =

Total plant-mediated C stocks can be accurately estimated using UAV-LiDAR in combination with machine learning regression methods at the ecosystem scale. These estimates correspond to cumulative $CO_2$ fluxes uptaken during the crop development. The match between the temporal development in C uptake in the footprint of the EC tower using the UAV-LiDAR based method and the eddy-covariance estimates showed an optimal mean error of $2.5 \pm 10.4$ % (in spring barley), and of $-9.0 \pm 13.3$ % (in winter wheat), finding that the comparisons of C stocks over the entire growing season (i.e. considering the first survey as reference date) resulted to be the most accurate ones.

However, it is crucial to consider that UAV-LiDAR estimates of C uptake may exhibit substantial over- or underestimation under certain conditions. This can occur when (i) LiDAR surveys are too close to one another, particularly during the later stages of phenological development, and (ii) a sample selection bias is introduced. For instance, it can be noted a positive bias on the 17 and 24 June 2021 (Figure 9), resulting in consistent overestimations in any comparison where these two dates are considered (Figure 10, b). Therefore, care must be taken as regards allowing suitable time intervals between surveys and appropriate AGC sampling schemes.

When comparing the resulting plant-C values with eddy-covariance estimates, a satisfactory level of agreement is observed, provided that the effects of AGC sampling design and time interval between UAV-LiDAR survey dates are taken into account. Conversely, $root_C$ is highly influenced by management practices and environmental factors throughout the growing season. Consequently, $root_C$ contributes significantly to the uncertainty in plant carbon estimates derived from UAV-LiDAR data.

We consider these results a promising step towards the data-driven upscaling of directly measured fluxes during the growing season in managed ecosystems, as well as towards the interpolation of $CO_2$ fluxes across eddy-covariance stations by leveraging mobile platforms and LiDAR technology.

## = Author contributions =

Original conceptual framework: TF, KT, JCR ; experimental design: KT, TF, JCR; UAV-LiDAR data collection: JCR, KT; field-based data collection and curation: RJ, JCR, KT; laser data processing: JCR, KT; eddy-covariance data collection and processing: RJ, TF, JCR; feature engineering, machine learning models' training and evaluation: JCR; visualisation: JCR and PR; project supervision: TF, KT; project administration: TF, KT; writing—original draft preparation: JCR; writing—review and editing: JCR, PR, TF, KT.

All contributing authors have read and agreed to the published version of the manuscript.

## = Acknowledgements =

The authors acknowledge the contributions of René Lee, Lars Rasmussen, Rune Skov Maigoord, Binsheng Gao, and Alek Wieckowski, in supporting the tasks of field-data acquisition, contributing to this study as fieldwork and laboratory assistants.

## = Funding =

This project has received funding support from the Talent Program Horizon 2020/Marie Skłodowska-Curie Actions, a Villum Experiment grant by the Velux Foundations, DK (MapCland project, project number: 00028314), the DeepCrop project (UCPH Strategic plan 2023 Data + Pool), as well as a UAS- ability infrastructure grant from Danish Agency for Science, Technology and Innovation. The authors acknowledge as well financial support from ICOS.

## List of abbreviations

- AGB: above-ground biomass.
- AGC: above-ground carbon.
- EC: eddy-covariance.
- ECB: ecosystem carbon balance.
- ERT: extreme randomized trees.
- GHG: greenhouse gas.
- GPP: gross primary productivity.
- ICOS: integrated carbon observation system.
- LiDAR: light detection and ranging.
- ML: machine learning.
- NECB: net ecosystem carbon balance.
- NEE: net ecosystem exchange.
- NPP: net primary productivity.
- PCD: point cloud data.

- $R_a$: autotrophic plant respiration.
- $R_{eco}$: ecosystem respiration.
- RF: random forest.
- $R_h$: heterotrophic respiration.
- $root_C$: carbon content in roots.
- Rsoil: microbial soil respiration.
- RS: remote sensing.
- $soil_C$: soil rhizodeposition.
- UAV: unstaffed aerial vehicle.
- WDI: water deficit index.
- $X_{ph}$: crops growth stage (according to Zadoks decimal code).

## Annex I: NEE, NPP, GPP, $R_{eco}$ in both growing seasons (2020 and 2021)

Figure 11 displays the processed NEE over time for both years, with a 30-minute pixel resolution. It ca be noted that in the 2020 season, there was an advancement of approximately 15 days, and more concentrated C uptake hotspots between 11:00 and 14:00 in late June and late July compared to the 2021 season.

Remarkably, in Figure 12, it can be observed that the time series of cumulative NPP and $R_{eco}$ never cross each other in 2021 (b), while they do so in 2020 (a). The enclosed area under these two curves indicates the rate of C accumulation efficiency with respect to ecosystem respiratory losses. It makes sense that in a more homogeneous, densely populated crop, the C uptake was more efficient than in the sparse crops of 2021.

These observations are consistent with the AGC sampling campaigns—where more sparse crops were sampled in the second year—and with the PCD representation of the cropfields (Figure 3)— where a higher PCD porosity was found in the second year as well as a lower cumulative NPP flux (Figure 9).

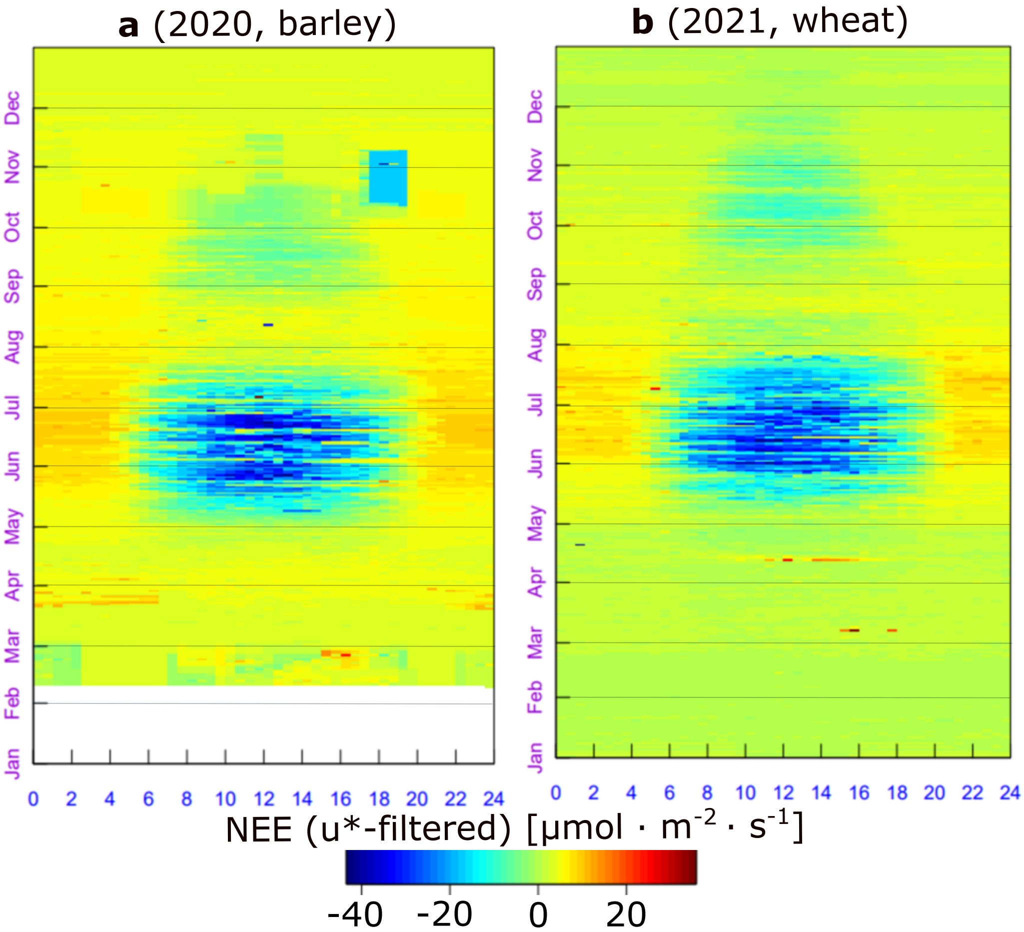


**Figure 11.** Measured net ecosystem exchange (NEE) at Voulundgaard research station during 2020 (**a**) and 2021 (**b**). Data displayed were gap-filled, spikes removed and u*-filtered. It can be noted a delay in the onset of the growing season in 2021 with respect to 2020 of almost 3 weeks, including a false start in mid May, partly explained by the cold spell of 10-12$^{th}$ February (figure obtained from the REddyProcWeb online tool : www.bgc-jena.mpg.de/bgi/index.php/Services/REddyProcWeb.

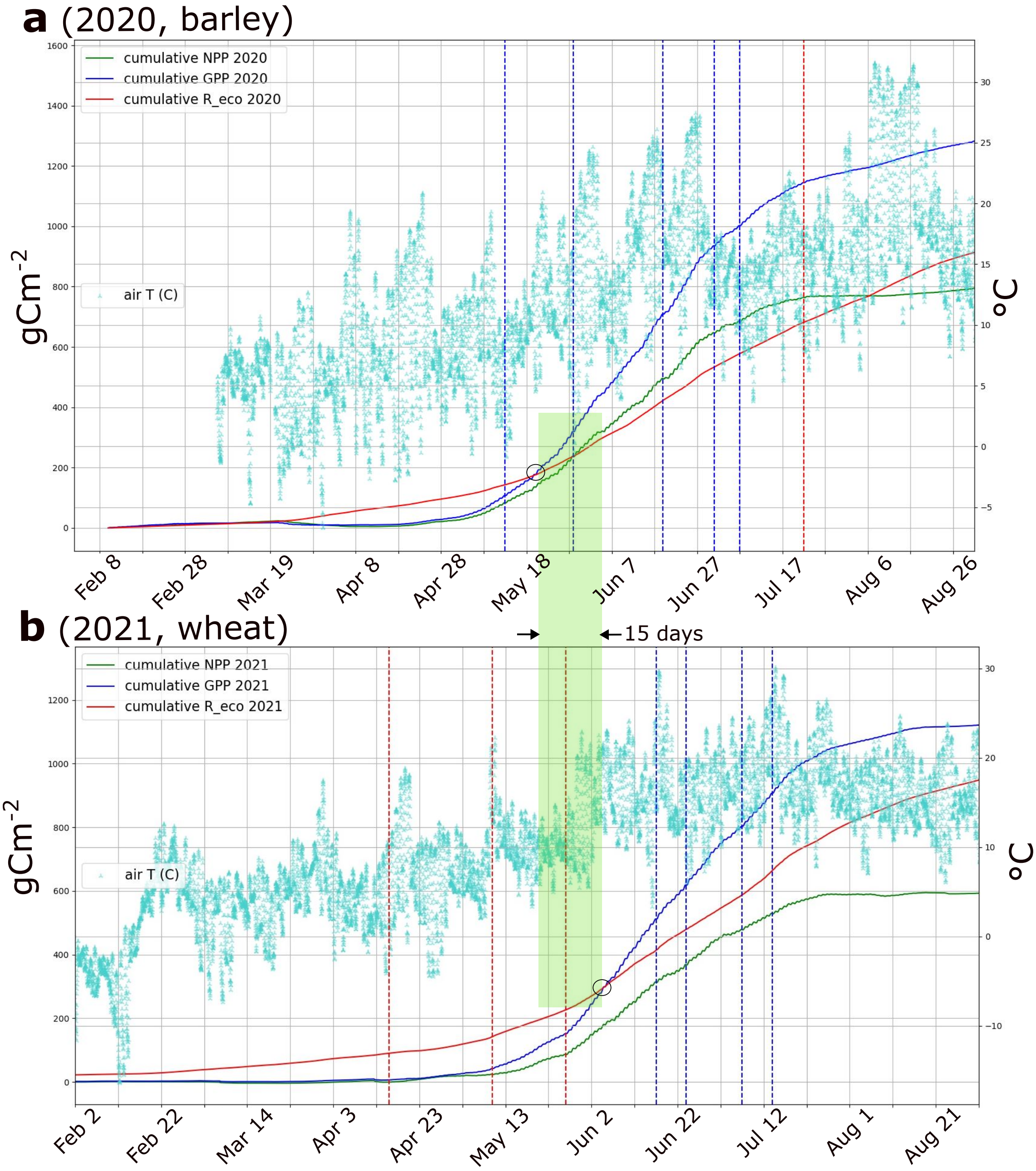


**Figure 12.** Estimated cumulative fluxes along the growing season of 2020 (**a**), and 2021 (**b**). GPP: gross primary productivity; $R_{eco}$: ecosystem respiration; NPP: net primary productivity. The red vertical lines indicate above-ground biomass (AGB) sampling dates, while the blue lines indicate dates in which both AGB sampling and UAV-LiDAR surveys took place. In both years, the black circles indicate the dates when GPP offsets $R_{eco}$. It can be observed how in 2021 this occurs on the $5^{th}$ June, while in 2020 GPP reaches ecosystem respiratory losses on the $19^{th}$ May, i.e. 16 days earlier. This delay in GPP during 2021 is partly explained due to the cold spell of February, damaging the early seedlings. The lack of temperatures at the beginning of 2020 (**a**) is due to a failure in the instrumental setup.

## References


[1] David Laborde et al. “Agricultural subsidies and global greenhouse gas emissions”. In: *Nature communications* 12.1 (2021), p. 2601.

[2] John R Porter, Mark Howden, and Pete Smith. “Considering agriculture in IPCC assessments”. In: *Nature Climate Change* 7.10 (2017), pp. 680–683.

[3] Philip Thornton et al. “Agriculture in a changing climate: Keeping our cool in the face of the hothouse”. In: *Outlook on Agriculture* 47.4 (2018), pp. 283–290.

[4] P. R. Shukla et al. *Summary for policymakers, in Climate Change Land: An IPCC Special Report on Climate Change Desertification, Land Degradation, Sustainable Land Management, Food Security, Greenhouse Gas Fluxes in Terrestrial Ecosystems*. Tech. rep. Intergovernmental Panel on Climate Change, 2023.

[5] Marco Springmann et al. “Options for keeping the food system within environmental limits”. In: *Nature* 562.7728 (2018), pp. 519–525.

[6] Gerald C Nelson et al. “Climate change effects on agriculture: Economic responses to biophysical shocks”. In: *Proceedings of the National Academy of Sciences* 111.9 (2014), pp. 3274–3279.

[7] David J Mulla. “Twenty five years of remote sensing in precision agriculture: Key advances and remaining knowledge gaps”. In: *Biosystems engineering* 114.4 (2013), pp. 358–371.

[8] Mitchell C Hunter et al. “Agriculture in 2050: recalibrating targets for sustainable intensification”. In: *Bioscience* 67.4 (2017), pp. 386–391.

[9] Hamid El Bilali et al. “Food and nutrition security and sustainability transitions in food systems”. In: *Food and energy security* 8.2 (2019), e00154.

[10] Jonathan A Foley et al. “Solutions for a cultivated planet”. In: *Nature* 478.7369 (2011), pp. 337–342.

[11] Tara Garnett et al. “Sustainable intensification in agriculture: premises and policies”. In: *Science* 341.6141 (2013), pp. 33–34.

[12] F Stuart Chapin, PA Matson, and PM Vitousek. *Principles of terrestrial ecosystem ecology. Principles of Terrestrial Ecosystem Ecology*. 2012.

[13] YM Zhang et al. “Vegetation carbon sequestration in the Loess Plateau under the synergistic effects of land cover change and elevations”. In: *Acta Ecologica Sinica* 42.10 (2022), pp. 3897–3908.

[14] Ulises Mariano Marconato, Roberto J Fernández, and Gabriela Posse Beaulieu. *Cropland Net Ecosystem Exchange Estimation for the Inland Pampas (Argentina) Using EVI, Land Cover Maps, and Eddy Covariance Fluxes*. Tech. rep. Frontiers Media, 2022.

[15] Arne Poyda et al. “Carbon fluxes and budgets of intensive crop rotations in two regional climates of southwest Germany”. In: *Agriculture, Ecosystems & Environment* 276 (2019), pp. 31–46.

[16] Anne-Katrin Prescher, Thomas Grünwald, and Christian Bernhofer. “Land use regulates carbon budgets in eastern Germany: From NEE to NBP”. In: *Agricultural and Forest Meteorology* 150.7-8 (2010), pp. 1016–1025.

[17] Rasmus Jensen, Mathias Herbst, and Thomas Friborg. *Direct and indirect controls of the interannual variability in atmospheric CO2 exchange of three contrasting ecosystems in Denmark*. 2016.

[18] Peter M Anthoni et al. "Winter wheat carbon exchange in Thuringia, Germany". In: *Agricultural and Forest Meteorology* 121.1-2 (2004), pp. 55–67.

[19] Praveena Krishnan et al. "Factors controlling the interannual variability in the carbon balance of a southern boreal black spruce forest". In: *Journal of Geophysical Research: Atmospheres* 113.D9 (2008).

[20] Christopher B Field and Jörg Kaduk. "The carbon balance of an old-growth forest: building across approaches". In: *Ecosystems* 7 (2004), pp. 525–533.

[21] Mark E Harmon et al. "Production, respiration, and overall carbon balance in an old-growth Pseudotsuga-Tsuga forest ecosystem". In: *Ecosystems* 7 (2004), pp. 498–512.

[22] Heather Keith, Brendan G Mackey, and David B Lindenmayer. "Re-evaluation of forest biomass carbon stocks and lessons from the world's most carbon-dense forests". In: *Proceedings of the National Academy of Sciences* 106.28 (2009), pp. 11635–11640.

[23] Scott D Miller et al. "Biometric and micrometeorological measurements of tropical forest carbon balance". In: *Ecological Applications* 14.sp4 (2004), pp. 114–126.

[24] Jian Wu et al. "Synthesis on the carbon budget and cycling in a Danish, temperate deciduous forest". In: *Agricultural and Forest Meteorology* 181 (2013), pp. 94–107.

[25] Thomas Foken, Marc Aubinet, and Ray Leuning. "The eddy covariance method". In: *Eddy covariance: a practical guide to measurement and data analysis*. Springer, 2011, pp. 1–19.

[26] Helene Hoffmann et al. "Crop water stress maps for an entire growing season from visible and thermal UAV imagery". In: *Biogeosciences* 13.24 (2016), pp. 6545–6563.

[27] Derek Hollenbeck and YangQuan Chen. "Multi-UAV method for continuous source rate estimation of fugitive gas emissions from a point source". In: *2021 International Conference on Unmanned Aircraft Systems (ICUAS)*. IEEE. 2021, pp. 1308–1313.

[28] Derek Hollenbeck et al. "Evaluating a UAV-based mobile sensing system designed to quantify ecosystem-based methane". In: *Authorea Preprints* (2022).

[29] Sheng Wang et al. "Temporal interpolation of land surface fluxes derived from remote sensing–results with an unmanned aerial system". In: *Hydrology and Earth System Sciences* 24.7 (2020), pp. 3643–3661.

[30] Jaime C Revenga et al. "Above-Ground Biomass Prediction for Croplands at a Sub-Meter Resolution Using UAV–LiDAR and Machine Learning Methods". In: *Remote Sensing* 14.16 (2022), p. 3912.

[31] N Ace Pugh et al. "Temporal estimates of crop growth in sorghum and maize breeding enabled by unmanned aerial systems". In: *The Plant Phenome Journal* 1.1 (2018), pp. 1–10.

[32] Wang Li et al. "Remote estimation of canopy height and aboveground biomass of maize using high-resolution stereo images from a low-cost unmanned aerial vehicle system". In: *Ecological indicators* 67 (2016), pp. 637–648.

[33] Abdullah M Al-Sadi et al. "Genetic analysis reveals diversity and genetic relationship among Trichoderma isolates from potting media, cultivated soil and uncultivated soil". In: *BMC microbiology* 15 (2015), pp. 1–11.

[34] Sebastian Varela et al. "Spatio-temporal evaluation of plant height in corn via unmanned aerial systems". In: *Journal of Applied Remote Sensing* 11.3 (2017), pp. 036013–036013.

[35] J Bendig et al. "Very high resolution crop surface models (CSMs) from UAV-based stereo images for rice growth monitoring in Northeast China". In: *Int. Arch. Photogramm. Remote Sens. Spat. Inf. Sci* 40 (2013), pp. 45–50.

[36] Juliane Bendig et al. "Estimating biomass of barley using crop surface models (CSMs) derived from UAV-based RGB imaging". In: *Remote sensing* 6.11 (2014), pp. 10395–10412.

[37] Sebastian Brocks and Georg Bareth. "Estimating barley biomass with crop surface models from oblique RGB imagery". In: *Remote Sensing* 10.2 (2018), p. 268.

[38] Tianxing Chu et al. "Cotton growth modeling and assessment using unmanned aircraft system visual-band imagery". In: *Journal of Applied Remote Sensing* 10.3 (2016), pp. 036018–036018.

[39] T Jensen et al. "Detecting the attributes of a wheat crop using digital imagery acquired from a low-altitude platform". In: *Computers and electronics in agriculture* 59.1-2 (2007), pp. 66–77.

[40] E Raymond Hunt et al. "NIR-green-blue high-resolution digital images for assessment of winter cover crop biomass". In: *GIScience & remote sensing* 48.1 (2011), pp. 86–98.

[41] Maria Tattaris, Matthew P Reynolds, and Scott C Chapman. "A direct comparison of remote sensing approaches for high-throughput phenotyping in plant breeding". In: *Frontiers in plant science* 7 (2016), p. 1131.

[42] Jakob Geipel et al. "A programmable aerial multispectral camera system for in-season crop biomass and nitrogen content estimation". In: *Agriculture* 6.1 (2016), p. 4.

[43] Jibo Yue et al. "Estimation of winter wheat above-ground biomass using unmanned aerial vehicle-based snapshot hyperspectral sensor and crop height improved models". In: *Remote Sensing* 9.7 (2017), p. 708.

[44] Roope Näsi et al. "Estimating biomass and nitrogen amount of barley and grass using UAV and aircraft based spectral and photogrammetric 3D features". In: *Remote Sensing* 10.7 (2018), p. 1082.

[45] Angela Kross et al. "Assessment of RapidEye vegetation indices for estimation of leaf area index and biomass in corn and soybean crops". In: *International Journal of Applied Earth Observation and Geoinformation* 34 (2015), pp. 235–248.

[46] Kishore C Swain, Steven J Thomson, and Hemantha PW Jayasuriya. "Adoption of an unmanned helicopter for low-altitude remote sensing to estimate yield and total biomass of a rice crop". In: *Transactions of the ASABE* 53.1 (2010), pp. 21–27.

[47] Jordan Steven Bates et al. "Estimating canopy density parameters time-series for winter wheat using UAS Mounted LiDAR". In: *Remote Sensing* 13.4 (2021), p. 710.

[48] ICOS. *Integrated Carbon Observation System*. 2023. URL: https://www.icos-cp.eu/ (visited on 02/04/2023).

[49] Danish Ministry of Environment. *Order on the use of fertilisers by agriculture for the 2020/2021 planning period*. 2021. URL: https://www.retsinformation.dk/eli/lta/2020/1166. (accessed: 25.10.2021).

[50] L Davidson et al. "Airborne to UAS LiDAR: An analysis of UAS LiDAR ground control targets". In: *ISPRS Geospatial Week 2019* (2019).

[51] Bert Gielen et al. "Ancillary vegetation measurements at ICOS ecosystem stations". In: *International Agrophysics* 32.4 (2018), pp. 645–664.

[52] Johanna Pausch and Yakov Kuzyakov. "Carbon input by roots into the soil: quantification of rhizodeposition from root to ecosystem scale". In: *Global change biology* 24.1 (2018), pp. 1–12.

[53] J Swinnen, JA Van Veen, and RJSB Merckx. "14C pulse-labelling of field-grown spring wheat: an evaluation of its use in rhizosphere carbon budget estimations". In: *Soil Biology and Biochemistry* 26.2 (1994), pp. 161–170.

[54] Erick Zagal, Sigfus Bjarnason, and ULF Olsson. "Carbon and nitrogen in the root-zone of barley (Hordeum vulgare L.) supplied with nitrogen fertilizer at two rates". In: *Plant and Soil* 157 (1993), pp. 51–63.

[55] PJ Gregory and BJ Atwell. "The fate of carbon in pulse-labelled crops of barley and wheat". In: *Plant and Soil* 136 (1991), pp. 205–213.

[56] Jan C Zadoks, Ting T Chang, Cal F Konzak, et al. "A decimal code for the growth stages of cereals." In: *Weed research* 14.6 (1974), pp. 415–421.

[57] Dean Vickers and L Mahrt. "Quality control and flux sampling problems for tower and aircraft data". In: *Journal of atmospheric and oceanic technology* 14.3 (1997), pp. 512–526.

[58] E. K. Webb, G. I. Pearman, and R. Leuning. "Correction of flux measurements for density effects due to heat and water vapour transfer". In: *Quarterly Journal of the Royal Meteorological Society* 106.447 (1980), pp. 85–100.

[59] Claudia Liebethal and Thomas Foken. "On the significance of the Webb correction to fluxes". In: *Boundary-Layer Meteorology* 109 (2003), pp. 99–106.

[60] JB Moncrieff et al. "A system to measure surface fluxes of momentum, sensible heat, water vapour and carbon dioxide". In: *Journal of Hydrology* 188 (1997), pp. 589–611.

[61] S Sabbatini and D Papale. *ICOS Ecosystem Instructions for Turbulent Flux Measurements of CO2, Energy and Momentum (Version 20180110), ICOS Ecosystem Thematic Centre*. 2017.

[62] Dario Papale et al. "Towards a standardized processing of Net Ecosystem Exchange measured with eddy covariance technique: algorithms and uncertainty estimation". In: *Biogeosciences* 3.4 (2006), pp. 571–583.

[63] Markus Reichstein et al. "On the separation of net ecosystem exchange into assimilation and ecosystem respiration: review and improved algorithm". In: *Global change biology* 11.9 (2005), pp. 1424–1439.

[64] Natascha Kljun, MW Rotach, and HP Schmid. "A three-dimensional backward Lagrangian footprint model for a wide range of boundary-layer stratifications". In: *Boundary-Layer Meteorology* 103 (2002), pp. 205–226.

[65] John Lloyd and JA Taylor. "On the temperature dependence of soil respiration". In: *Functional ecology* (1994), pp. 315–323.

[66] Peter J Huber. "Robust statistics". In: *International encyclopedia of statistical science*. Springer, 2011, pp. 1248–1251.

[67] Art B Owen. "A robust hybrid of lasso and ridge regression". In: *Contemporary Mathematics* 443.7 (2007), pp. 59–72.

[68] Pierre Geurts, Damien Ernst, and Louis Wehenkel. "Extremely randomized trees". In: *Machine learning* 63.1 (2006), pp. 3–42.

[69] Tianqi Chen et al. "Xgboost: extreme gradient boosting". In: *R package version 0.4-2* 1.4 (2015), pp. 1–4.

[70] Leo Breiman. "Random forests". In: *Machine learning* 45.1 (2001), pp. 5–32.

[71] Teng Hu et al. "Root biomass in cereals, catch crops and weeds can be reliably estimated without considering aboveground biomass". In: *Agriculture, Ecosystems & Environment* 251 (2018), pp. 141–148.

[72] Yakov Kuzyakov and Grzegorz Domanski. "Carbon input by plants into the soil. Review". In: *Journal of Plant Nutrition and Soil Science* 163.4 (2000), pp. 421–431.

[73] JA Palta and PJ Gregory. "Drought affects the fluxes of carbon to roots and soil in 13C pulse-labelled plants of wheat". In: *Soil Biology and Biochemistry* 29.9-10 (1997), pp. 1395–1403.

[74] Ernest C Large et al. "Growth stages in cereals. Illustration of the Feekes scale." In: *Plant pathology* 3 (1954), pp. 128–129.

[75] Ngonidzashe Chirinda, Jørgen E Olesen, and John R Porter. "Root carbon input in organic and inorganic fertilizer-based systems". In: *Plant and Soil* 359 (2012), pp. 321–333.

[76] Shai Ben-David et al. "A theory of learning from different domains". In: *Machine learning* 79 (2010), pp. 151–175.

[77] Joaquin Quinonero-Candela et al. *Dataset shift in machine learning*. Mit Press, 2008.

[78] Afshin Soltani. *Modeling physiology of crop development, growth and yield*. CABi, 2012.